High-Performance Electrochemical Immunosensors Based on La_2O_3/g-C_3N_4 and SiO_2/g-C_3N_4 Nanocomposites: A Mechanistic Comparative Study for AFP Detection

Samiksha Antil[1], Pooja Rahar[2], Jyoti Rani[2], Saravjeet Singh[*]
[1,2]Department of Biomedical Engineering, Deenbandhu Chhotu Ram University of Science and Technology, Murthal 131039, India
***Corresponding Author**
Email: saravjeet.bme@dcrustm.org
Received: 5th May, 2026; **Revised:** 22nd June, 2026; **Accepted:** 16th July, 2026; **Available Online:** 26th July, 2026

ABSTRACT
Early diagnosis of hepatic carcinoma remains challenging due to the low concentrations of AFP and the inadequate sensitivity of existing diagnostic techniques. This paper presents a comparative analysis of the mechanism of label-free electrochemical AFP immunosensors developed from La_2O_3/g-C_3N_4 (LCN) and SiO_2/g-C_3N_4 (SCN) nanocomposites. The immune-sensors were fabricated by screen-printing carbon electrodes onto a paper substrate, subsequently incorporating anti-AFP antibodies for selective detection and signal transduction. The electrochemical characteristics were evaluated using cyclic voltammetry (CV) and electrochemical impedance spectroscopy (EIS) techniques. The results obtained reveal several sensing mechanisms governed by the chemistry of oxides. Consequently, La_2O_3 assists in the heterogeneous electron transfer process via charge transfer mechanism, whereas SiO_2 serves to immobilize antibodies and enhance signals due to its high silanol concentration and porous architecture. The SCN immunosensor demonstrates superior analytical performance with a linear range of 0.25-500 ng/mL and a limit of detection (LOD) of 0.0024 ng/mL, whereas the LCN immunosensor exhibits a LOD of 0.035 ng/mL. The results show that both sensors demonstrated improved selectivity, repeatability (RSD $\leq$ 3.98%), and stability over a period of 28 days.
Keywords: Alpha-fetoprotein (AFP); Lanthanum oxide; Silicon dioxide; Graphitic carbon nitride; Electrochemical immunosensor; Hepatocellular carcinoma.
How to cite this article: Antil S, Rahar P, Rani J, Singh S. High-Performance Electrochemical Immunosensors Based on La2O3/g-C3N4 and SiO2/g-C3N4 Nanocomposites: A Mechanistic Comparative Study for AFP Detection. Int J Drug Deliv Technol. 2026;16(72s): 1061-1074. DOI: 10.25258/ijddt.16.72s.117

Source of support: Nil.
Conflict of interest: Nil

INTRODUCTION

Hepatocellular carcinoma (HCC) is the predominant form of primary liver cancer, encompassing approximately 75-85% of all hepatic malignancies and significantly contributing to global cancer mortality rates [1,2]. Hepatocellular carcinoma (HCC) is associated with various chronic liver diseases, including hepatitis B and C virus infections, as well as alcoholic and non-alcoholic fatty liver disease [3]. The prognosis for patients is primarily dependent upon the stage of the disorder at the time of diagnosis, despite numerous advancements in treatment methodologies.

Alpha-fetoprotein (AFP) is a 70 kDa glycoprotein, expressed during fetal liver development and functions as a serum biomarker for assessing hepatocellular carcinoma (HCC) tumor growth rate. The circulating blood level of AFP in healthy individuals is below 10 ng/mL, but the serum AFP level rises significantly in patients diagnosed with HCC [4]. The expression of AFP can vary considerably and may increase in many physiological conditions, including hepatitis and liver cirrhosis [5].

Electrochemical immunosensors have recently emerged as promising alternatives to traditional immunoassay techniques due to their rapid response, minimal sample requirements, ease of use, and suitability for point-of-care testing [6,7]. The label-free detection method enables the processing of antigen-antibody complex binding events into an electrochemical signal via changes in the charge transfer capacity of the electrode surface. The sensitivity and selectivity of electrochemical sensors are significantly impacted by the physical and chemical characterstics of the modified electrode surface [8]. Graphitic carbon nitride (g-C_3N_4) has attracted significant interest in academic research as a potential biosensor material due to its exceptional chemical stability and biocompatibility [9,10]. The structural configuration of g-C_3N_4 offers several reactive sites that enable interactions with biological molecules and promote signal propagation. Nevertheless, g-C_3N_4 exhibits relatively low electrical conductivity; thereby, it is crucial to incorporate the nanomaterial with other functionalized inorganic substances [11].

Among various modifiers, lanthanum oxide (La_2O_3)

and silicon dioxide (SiO_2) possess distinct advantages. La_2O_3 facilities charge transport through defect-based charge transfer processes and exhibits electrocatalytic activity, whereas silicon dioxide forms a chemically stable, high-surface-area matrix abundant in silanol groups, which helps in the immobilization of antibodies [12-15]. Despite the numerous publications regarding AFP biosensors using graphene, MXene, and metal oxides, a comparative analysis of the effect of oxides nano phase chemistry on g-C_3N_4 based immunosensors remains insufficiently conducted. A comparison among La_2O_3/g-C_3N_4 and SiO_2/g-C_3N_4 is unknown.

This study outlines a comparative analysis of the transduction mechanisms underlying La_2O_3/g-C_3N_4 (LCN) and SiO_2/g-C_3N_4 (SCN) immunoplatforms under similar experimental conditions, which advances further than previous work that focused on the sensing properties of these platforms independently. The performance of La_2O_3/g-C_3N_4 (LCN) and SiO_2/g-C_3N_4 (SCN) immunosensing devices in detecting AFP was comparatively analyzed. The impact of oxide chemistry on the mechanisms of charge transfer processes, antibody immobilization, and analysis was examined through CV, EIS, and DPV, utilizing a single platform for fabrication and analysis of both LCN and SCN. The research study demonstrates a direct correlation between oxide nanointerface chemistry and sensing performance. This provides useful information for prospective research focused on developing electrochemical immunosensors for hepatocellular carcinoma diagnosis.

2. Experimental Section

2.1. Chemicals and Reagents

Urea, tetraethyl orthosilicate (TEOS), ammonia solution (25-28%), ethanol, lanthanum powder, potassium chloride (KCl), potassium ferricyanide ($K_3[Fe(CN)_6]$), and potassium ferrocyanide trihydrate ($K_4[Fe(CN)_6]\cdot 3H_2O$) were purchased from Merck (India). AFP antigen and anti-AFP monoclonal antibodies were obtained from BTL Biotechno Labs Pvt. Ltd., India. N-(3-Dimethylaminopropyl)-N′-ethylcarbodiimide hydrochloride (EDC), bovine serum albumin (BSA), and cysteamine dihydrochloride were used for surface functionalization. Phosphate-buffered saline (PBS, 0.01 M, pH 7.4) was the supporting electrolyte for all immunoreactions. All chemicals were analytical grade and used without further purification; solutions were prepared in ultrapure Milli-Q water (18.2 MΩ.cm).

2.2. Nanocomposite Synthesis

The synthesis method for g-C_3N_4, La_2O_3 nanoparticles, SiO_2 nanoparticles, and their corresponding La_2O_3/g-C_3N_4 (LCN) and SiO_2/g-C_3N_4 (SCN) heteronanocomposites, have been thoroughly discussed in our previous papers [16,17]. G-C_3N_4 was synthesized using the thermal polycondensation of urea, whilst La_2O_3 and SiO_2 nanoparticles were produced using sol-gel and modified Stöber methods, respectively. The synthesized La_2O_3 and SiO_2 nanoparticles were ultimately integrated with g-C_3N_4 to form LCN and SCN heterocomposites. To enable a systematic evaluation of their properties, both composites were synthesized using a single batch of g-C_3N_4 under similar fabrication conditions. The quantity of g-C_3N_4 corresponds to the mass fraction of the oxide material (either La_2O_3 or SiO_2), and all phases of dispersion, drying, and thermal treatment were performed under identical conditions for each composite sample. This methodology reduced several elements that might affect the research outcomes, hence facilitating an analysis of the impact of oxides on the functionality of nanocomposites.

2.3. Immunosensor Fabrication

The procedures used in preparing LCN and SCN immune-sensors were based on protocols that had been described earlier [16,17]. Briefly, SPCE sensors on paper substrate were sequentially coated with cysteamine, the corresponding nanocomposites (LCN or SCN), anti-AFP antibody, and BSA as a blocking layer. The immobilization of antibodies was achieved through EDC/NHS chemistry. To ensure consistency in the analysis, similar materials, reagent concentrations, immobilization conditions, and incubation parameters were employed in both studies. Electrochemical tests were conducted with electrodes made uniformly to reduce fabrication variability, hence facilitating the investigation of the impact of nanophase oxide identity on immunosensing.

2.4. Electrochemical Measurements

Electrochemical study was conducted using a PalmSens4 potentiostat/galvanostat governed by PSTrace software, utilizing a 5mM $[Fe(CN)_6]^{3-/4-}$ redox mediator solution with 0.05 M KCl as the electrolyte, conducted at room temperature. The cyclic voltammetry (CV) was performed at a scan rate of 50 mV s^{-1}, while electrochemical impedance spectroscopy (EIS) was conducted at a frequency range from 10^{-1} to 10^5 Hz, utilizing a small amplitude AC modulation of 10 mV at open circuit potential (OCP). All studies were conducted thrice, and the findings were evaluated using one-way ANOVA ($p<0.05$).

3. Results and Discussion

3.1. Comparative Physicochemical Characterization

A comprehensive analysis of the physicochemical properties of LCN and SCN nanostructures has already been reported in our previous study. The current paper focuses on reporting the significant properties related to the process of charge transfer, immobilization of biomolecules, and immune-sensing capability.

3.1.1. Structural Analysis (XRD)

The X-ray diffraction (XRD) patterns of LCN and SCN are illustrated in figure 1.1. Both composites have the characteristic diffraction peaks of g-C_3N_4 at around 13.1° and 27.4°, indicating that the graphitic structure is maintained despite the incorporation of oxides [18]. The further peaks at around 28.4°, 32.6°, and 33.8° for LCN composites validate the effective synthesis of crystalline cubic La_2O_3 [19]. A broad diffraction peak at around 22° is evident in the SCN composite, indicating the presence of amorphous SiO_2 [20]. The inclusion of La_2O_3 and g-C_3N_4 in LCN indicates the successful fabrication of a heterojunction, whereas the presence of SiO_2 in SCN merely alters the surface morphology without affecting the crystal structure of g-C_3N_4. The disparity in structural composition has the potential to influence their charge-transfer characterstics and biological interactions in several ways.

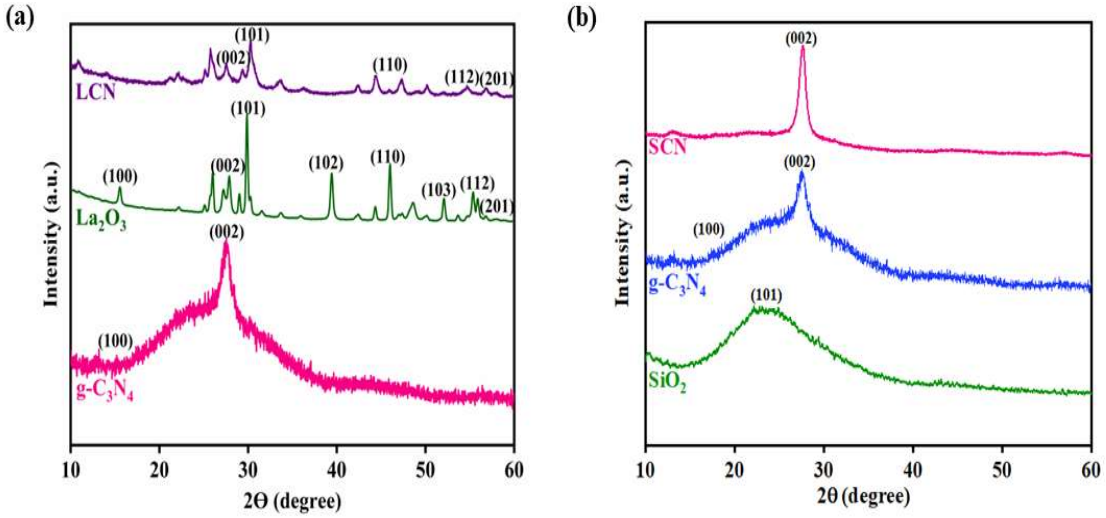

Figure 1.1. Comparative XRD patterns of g-C_3N_4, La_2O_3/ g-C_3N_4 (LCN) and SiO_2/g-C_3N_4 (SCN) nanocomposites.

3.1.2. Functional Group Analysis (FTIR)

The FTIR spectra of LCN and SCN nanocomposites are shown in Figure 1.2. Both nanocomposites exhibit distinct vibrational spectra of g-C_3N_4, characterized by vibration bands associated with C-N and C=N stretches in heterocyclic compounds within the 1200-1650 cm^{-1} range, as well as a vibration band corresponding to breathing vibrations in tri-s-triazine at 810 cm^{-1} [21]. In LCN, La-O vibrational peaks are observed between 340-854 cm^{-1}, but the positions of the vibrational peaks associated with g-C_3N_4 exhibit minimal variation [22]. Notably, significant broadening is observed in the triazine bands at approximately 1560, 1400, and 1300 cm^{-1}, accompanied by intensified O-H/N-H absorption in the range of 3300 to 3500 cm^{-1} [23]. This indicates that SiO_2 exhibits more stable interfacial interactions with g-C_3N_4 compared to LCN. The FTIR study results indicate the presence of a heterojunction between La_2O_3 and g-C_3N_4 in LCN, as well as a surface interaction between the SiO_2/g-C_3N_4 architecture in SCN.

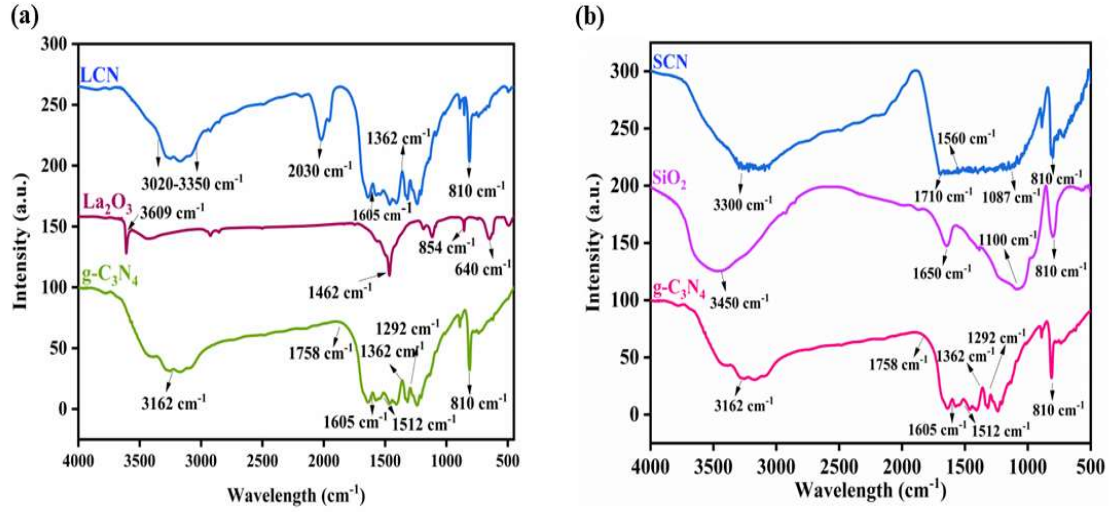

Figure 1.2. Comparative FTIR spectra of g-C_3N_4, La_2O_3/ g-C_3N_4 (LCN) and SiO_2/g-C_3N_4 (SCN) nanocomposites.

3.1.3. Optical Properties (UV-Visible Spectroscopy)

The UV-Vis absorption spectroscopy of La_2O_3, g-C_3N_4, SiO_2, SCN and LCN nanocomposites confirms their synthesis and shows enhanced optical characteristics in figure 1.3. The crystalline chemical La_2O_3 exhibits an absorption peak at 230 nm, whereas g-C_3N_4 displays absorption bands are around 220 nm and 245 nm, extending into the visible spectrum [24]. The absorption peak in SiO_2 is observed at 215 nm, attributed to Si-O-Si transitions. The absorption peak of the SCN nanocomposite is observed at around 220 nm, demonstrating enhanced absorbance relative to g-C_3N_4 [25]. The absorption peaks for the LCN nanocomposites were identified at around 230 nm and 350 nm.

The sample comprising La_2O_3 exhibits a minor red shift in its absorbance peak, accompanied by an enhancement in its visible light absorption efficiency, indicating electronic interaction between the two materials. Conversely, the sample including SiO_2 exhibits a minor blue shift in its absorbance peak, indicating the inclusion of amorphous SiO_2 with minimal disruption to the electronic structure of g-C_3N_4.

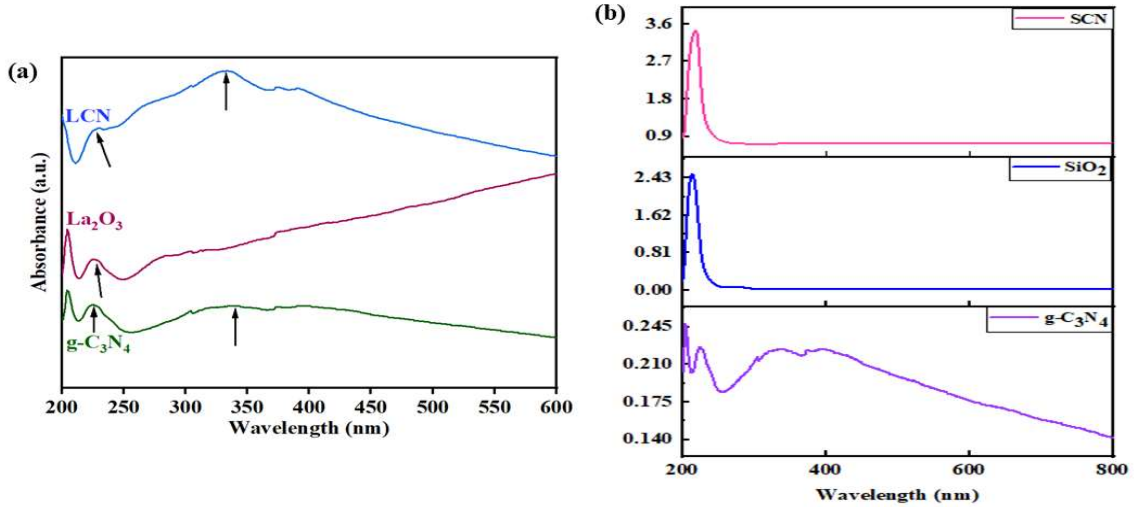

Figure 1.3. Comparative UV-Visible absorption spectra g-C_3N_4, La_2O_3/ g-C_3N_4 (LCN) and SiO_2/g-C_3N_4 (SCN) nanocomposites.

3.1.4 FESEM Morphological Analysis

Figure 1.4 shows the FESEM images of g-C_3N_4, La_2O_3, SiO_2, LCN, and SCN. The g-C_3N_4 displays a recognized morphology characterized by layered, wrinkled sheets of graphitic carbon nitride synthesized via thermal process, offering significant surface area for nano-phase integration [26]. La_2O_3 nanocrystals exhibit uniformity and a quasi-spherical morphology with dense packing, whereas SiO_2 possesses an amorphous structure [27].

After the synthesis of the composite materials, the LCN heterojunction observed uniform attachment of La_2O_3 nanoparticles to the g-C_3N_4 layers, thereby resulting in close interface interaction and effective distribution of the oxide component within the carbon nitride particles both on and between the g-C_3N_4 nanosheets, resulting in an open and porous surface morphology due to the increased sheet separation distance. The morphologies of the two composite methods exhibit a clear distinction, where the LCN shows close oxide-support integration, while the SCN displays wide porosity attributed to silica inclusion.

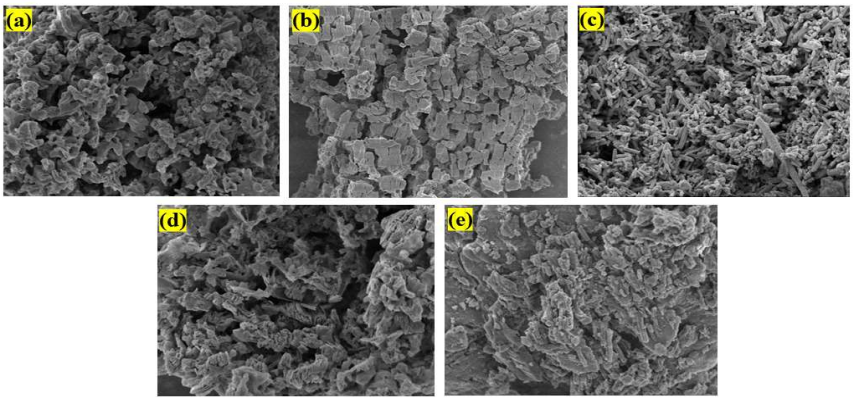

Figure 6.4. FESEM micrographs of (a) g-C_3N_4, (b) La_2O_3 nanoparticles, (c) SiO_2 nanoparticles, (d) La_2O_3/ g-C_3N_4 (LCN), and (e) SiO_2/g-C_3N_4 (SCN) nanocomposites.

3.1.5 Elemental Composition Analysis (EDX)

EDX spectra of the individual component and corresponding nanocomposite materials are illustrated in Figure 1.5. EDX spectrum of g-C_3N_4 material (Figures 1.5 (b) and 1.5 (e)) shows peaks which belong only to C and N elements, confirming that the material is composed of typical graphitic carbon nitride. On the other hand, EDX spectrum of La_2O_3 nanoparticles (Figure 1.5 (a)) exhibits dominant peak related to La and O elements, while SiO_2 nanoparticles (Figure 1.5d) display characteristic peaks of Si and O elements.

The presence of all three elements (La, C, and N) in the spectra depicted in Figure 1.5 (c) verifies the successful incorporation of La_2O_3 into the g-C_3N_4 framework. In addition, the occurrence of patterns corresponding to Si, O, C, and N atoms in the SCN spectra (Figure 1.5 (f)) further confirms the presence of SiO_2 and g-C_3N_4 inside the matrix. The absence of impurity peaks in both composites indicates excellent phase purity and effective incorporation of oxides inside the carbon nitride matrix, consistent with findings from XRD and FESEM analyses.

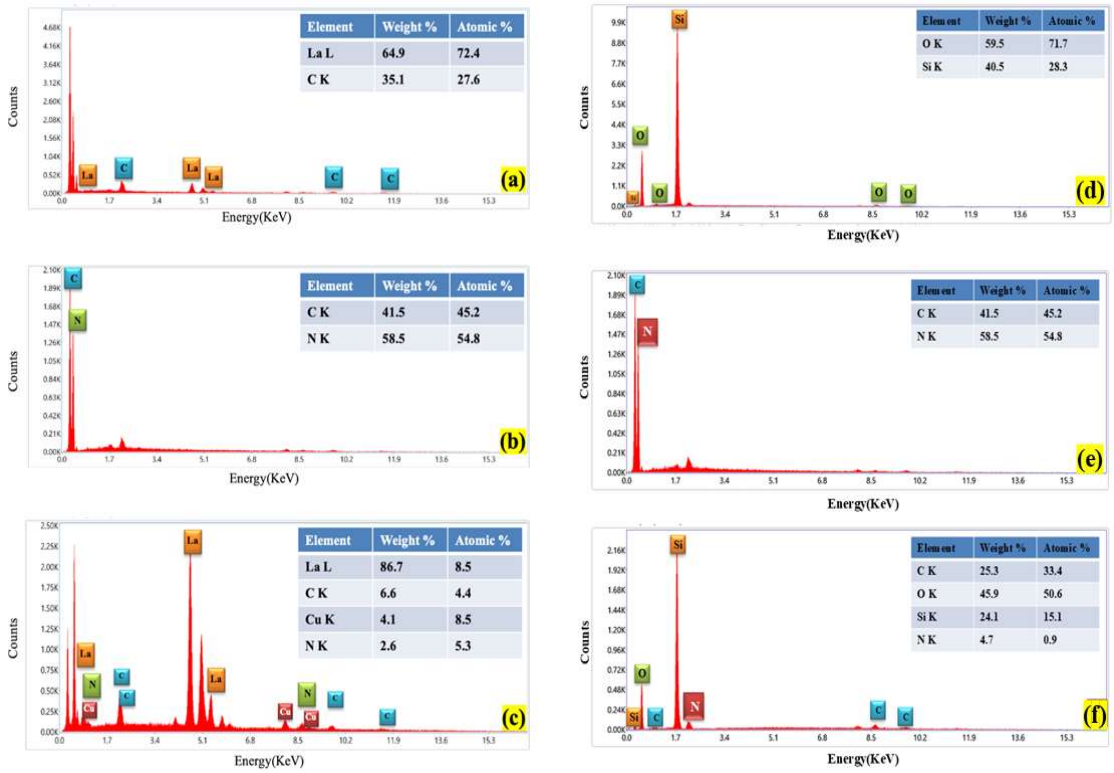

Figure 1.5. EDX spectra of (a) La_2O_3 nanoparticles, (b,e) g-C_3N_4, (c) La_2O_3/ g-C_3N_4 (LCN), (d) SiO_2 nanoparticles, and (f) SiO_2/g-C_3N_4 (SCN) nanocomposites.

Table 1.1. Comparative physicochemical characteristics of La_2O_3/ g-C_3N_4 (LCN), and SiO_2/g-C_3N_4 (SCN) nanocomposites.

Characterization Technique	Physicochemical Attribute	g-C_3N_4	LCN	SCN
XRD	Characteristic diffraction features	13.1°, 27.2°	g-C_3N_4 peaks retained; La_2O_3 reflections at 28.4°, 32.6°, 33.8°	g-C_3N_4 peaks retained; broad amorphous halo at ~22°
XRD	Structural architecture	Layered graphitic framework	Crystalline La_2O_3/g-C_3N_4 heterojunction	Amorphous SiO_2-decorated g-C_3N_4 network
XRD	Crystallite size	—	~8 nm (La_2O_3)	Amorphous
FTIR	Dominant interfacial interaction	—	Non-covalent oxide–support integration	Hydrogen bonding between Si–OH and g-C_3N_4
UV–Vis	Optical response	Absorption edge ~450 nm	Slight red shift; enhanced visible-light absorption	Marginal blue shift; minimal bandgap modulation
FESEM	Surface morphology	Aggregated lamellar nanosheets	Quasi-spherical La_2O_3 nanoparticles uniformly anchored on g-C_3N_4 sheets	Porous surface-decorated architecture with distributed SiO_2 clusters
EDS	Elemental composition	C, N	La, O, C, N	Si, O, C, N
Overall implication	Expected functional role	Conductive support matrix	Enhanced interfacial charge-transfer characteristics	Increased surface accessibility and biointerface functionality

4. Electrochemical characterization

4.1. Cyclic Voltammetry and Interfacial Electron - Transfer Behavior

The electrochemical performance of the LCN and SCN modified electrodes during the stepwise fabrication process of the immunosensor via cyclic voltammetry in a 5 mM $[Fe(CN)_6]^{3-/4-}$ solution containing 0.05 M KCl is illustrated in Figure 1.6. The performance of the two modifying strategies indicated that the deposition of the nanocomposites significantly enhanced the redox current with respect to the bare electrode, demonstrating improved electron transport at the interface. The enhancement of current was significantly stronger for the LCN-modified electrode, with an increase from 103.9 to 197.2 μA (about 89.8%), compared to the SCN-modified electrode, which exhibited an increase from 155.2 to 212.3 μA (approximately 36.8%).

The immobilization of anti-AFP antibodies on both sensing surfaces results in a reduction in peak currents for both systems, related to the formation of an insulating biorecognition layer which obstructed electron transport between the electrode surface and the electrolyte solution [28]. The result therefore validates both the immobilization method and the performance of the biosensing technology. In both sensor configurations, the ΔEp values diminished with the accelerated electron transport facilitated by heterojunction formation. The improved conductivity in LCN is primarily associated with heterojunction and defect-assisted electronic coupling processes, whereas the reduced ΔEp in SCN has been attributed to enhanced electrolyte accessibility.

The Randles-Sevcík model exhibited strong concordance with the experimental data in both instances (R^2 >0.99), allowing the analysis of electroactive surface area (EASA). For LCN, the EASA improved from 0.0098 to 0.0205 cm^2; conversely, the SCN electrodes exhibited markedly greater surface area (0.188-0.257 cm^2), with roughness factors of 0.289 and 3.64, respectively. This finding the distinctions between the two platforms concerning their operational principles, with LCN becoming primarily dependent on the conducive interaction at the heterojunction, while SCN functions due to its high surface-area-architecture.

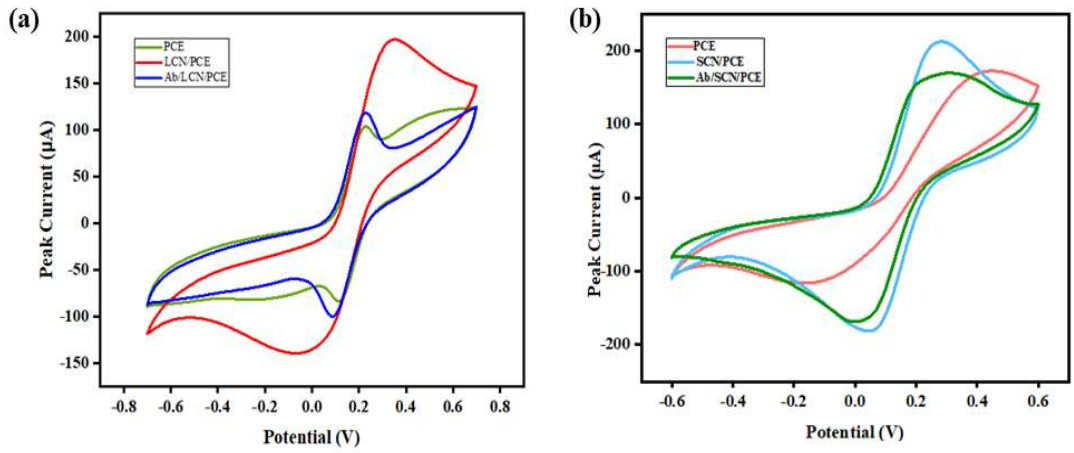

Figure 1.6. Cyclic Voltammetry recorded in 5mM $[Fe(CN)_6]^{3-/4-}$ containing 0.05 M KCl for (a) LCN-based and (b) SCN-based immunosensor during sequential fabrication.

4.2. Electrochemical Impedance Spectroscopy and Charge-Transfer Kinetics

The charge transfer properties at the interface were evaluated utilizing electrochemical impedance spectroscopy (EIS) with the $[Fe(CN)_6]^{3-/4-}$ redox couple (Fig. 1.7). A corresponding decrease in semicircle size was observed in both modified surfaces, indicating an enhancement in electron transport performance due to the reduction in Rct [29]. Nonetheless, this enhancement was not homogeneous throughout each sensor.

Following the modification using nanocomposites, the Rct of LCN possessed a substantial reduction of 60.1%, decreasing from 335.8 to 134.0 Ω. The resistance of SCN decreased from 946.9 to 534.4 Ω, indicating a reduction of 43.6%. The above result further supports the heterojunction configuration of La_2O_3/g-C_3N_4 facilitates more efficient charge transfer than the heterojunction configuration of SiO_2/g-C_3N_4. Kinetic experiments utilizing the Butler-Volmer equation reveal substantial enhancements in the rate constant of heterogeneous electron transfer (K_0) and exchange current density (i_0) of LCN, combined with i_0 increasing from 1.62×10^{-2} to 1.94×10^{-2} cm s^{-1}. The values for SCN were significantly lower, increasing by merely an order of magnitude form 7.9×10^{-4} to 1.4×10^{-3} cm s^{-1}.

The charge transfer resistance improved to 248.2 Ω for LCN and 715.9 Ω for SCN following the immobilization of the anti-AFP antibody, indicating the formation of an insulating biorecognition layer which partially restricts the redox probe's accessibility to the electrode interface. The increase in resistance for SCN significantly exceeds for LCN, a phenomenon attributed to the enhanced antibody coverage on SCN resulting from its porous structure and silanol functional groups.

The EIS studies demonstrated the mechanistic distinctions between the two nano-composites. The LCN enhances electrochemical capabilities by facilitating rapid transfer through electronic coupling from heterojunction formation, whilst SCN provides sensing advantages due to its bioactive surface area.

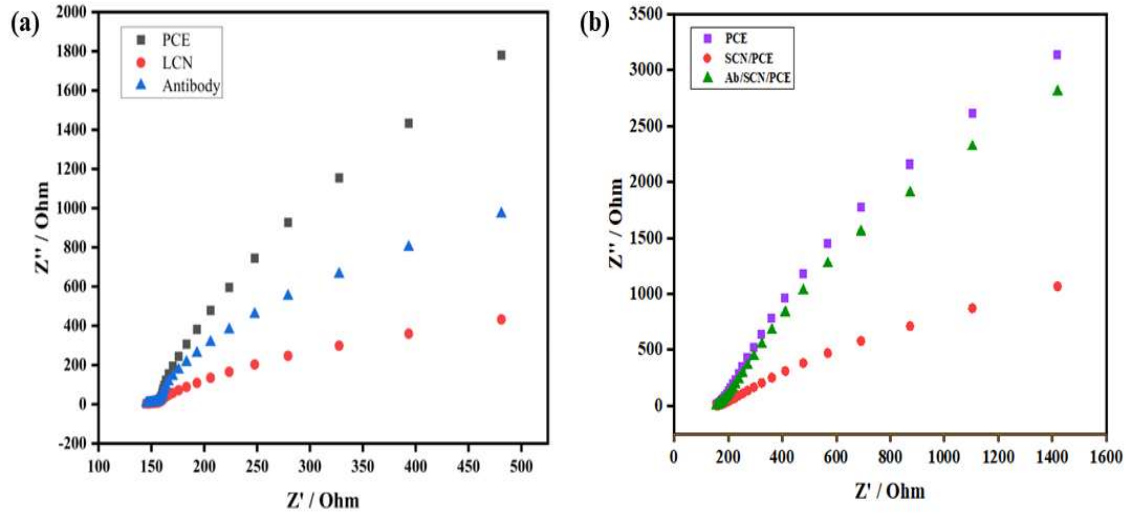

Figure 1.7. Nyquist plots of (a) LCN based and (b) SCN based immunoplatforms during sequential fabrication in 5mM $[Fe(CN)_6]^{3-/4-}$/0.05 M KCl.

Table 1.2. Comparative Electrochemical Parameters of LCN and SCN Immunosensor Platforms.

Parameter	Bare PCE (LCN)	LCN/PCE	Bare PCE (SCN)	SCN/PCE
Ip (CV, µA)	103.9	197.2 (+89.8%)	155.2	212.3 (+36.8%)
ΔEp (V)	0.38	0.32	0.44	0.27
Rct (Ω)	335.8	134.0 (−60.1%)	946.9	534.4 (−43.6%)
EASA (cm^2)	0.0098	0.0205 (2.1×)	0.188	0.257 (1.37×)
Roughness factor (Rf)	0.139	0.289	2.66	3.64
i_0 (A)	7.65×10^{-5}	1.92×10^{-4} (2.5×)	2.7×10^{-5}	4.8×10^{-5} (1.78×)
k_0 (cm s^{-1})	1.62×10^{-2}	1.94×10^{-2} (1.2×)	7.9×10^{-4}	1.4×10^{-3} (1.77×)
Post-Ab Rct (Ω)	—	248.2	—	715.9

4.3. Comparative AFP Detection and Calibration Characteristics

The electroanalytical performance of the LCN and SCN immunosensor system for detecting AFP within the range of 0.25-500 ng mL^{-1} was assessed using cyclic voltammetry (Figure 6.8). In both instances, elevated levels of AFP resulted in a reduction of the anodic peak current, indicating that the insulation of the immunocomplexes impeded the electron transfer mechanism of the ferri/ferrocyanide redox system at the electrode interface.

The LCN immunosensor demonstrated a linear correlation between peak currents and the logarithm of AFP values, represented as:

I_p = -28.44 log CAFP + 143.70

with the coefficient of determination is R^2 = 0.9959. LCN obtained a sensitivity of 28.44 μA/decade, a limit of detection (LOD) of 0.035 ng/mL, and a limit of quantification (LOQ) of 0.107 ng/mL. Conversely, SCN achieved a steeper calibration curve compared to LCN as detailed below:

I_p = -39.03 log C_AFP + 203.33,

Exhibiting superior linearity with R^2 = 0.9989. This immunosensor exhibited a sensitivity of 39.03 μA/decade, representing 37% increase compared to the LCN, despite maintaining a very low limit of detection (LOD) of 0.00224ng/mL and a limit of quantification (LOQ) of 0.00679 ng/mL.

The enhanced analytical performance of SCN is due to its porous structure, resulting in an increased electroactive surface area and facilitating antibody immobilization via a high density of silanol groups [30]. Consequently, AFP interaction significantly blocks electrolyte kinetics, leading to pronounced signal attenuation. For LCN sensor, sensing method is primarily influenced by the electron transfer rate across the La_2O_3/g-C_3N_4 heterojunction, resulting in efficient but considerably attenuated signal changes at extremely low AFP concentrations.

Both immunosensors exhibited significant consistency within a clinically applicable range of AFP values, encompassing normal conditions to the early and advanced stages of HCC. Nevertheless, SCN exhibited considerably higher sensitivity and approximately 16 times lower detection limits compared to kinetic-based sensing.

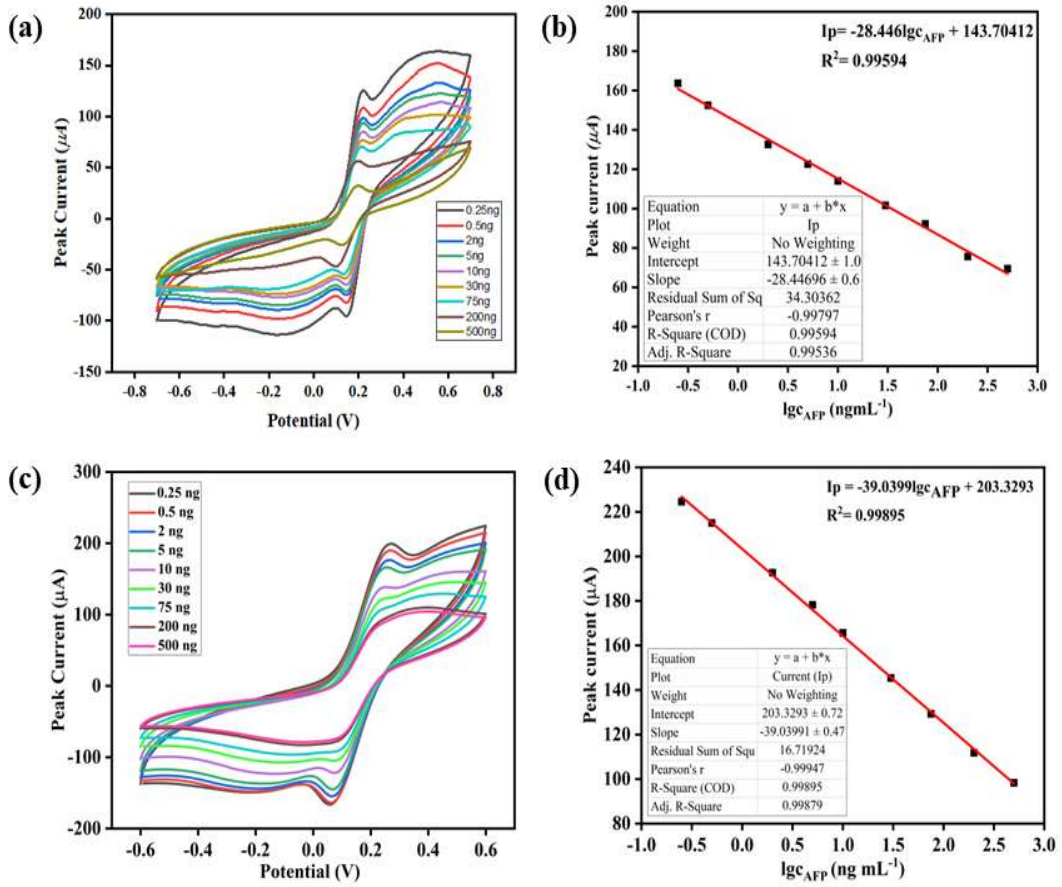

Figure 1.8. (a) CV responses and (b) corresponding calibration plot of the LCN immunosensor towards AFP (0.25-500 ng mL^{-1}). (c) CV responses and (d) corresponding calibration plot of the SCN immunosensor. Both platforms exhibit concentration-dependent current suppression upon AFP binding, with SCN demonstrating higher sensitivity and a lower detection limit than LCN.

4.4. Optimization of Operating Parameters

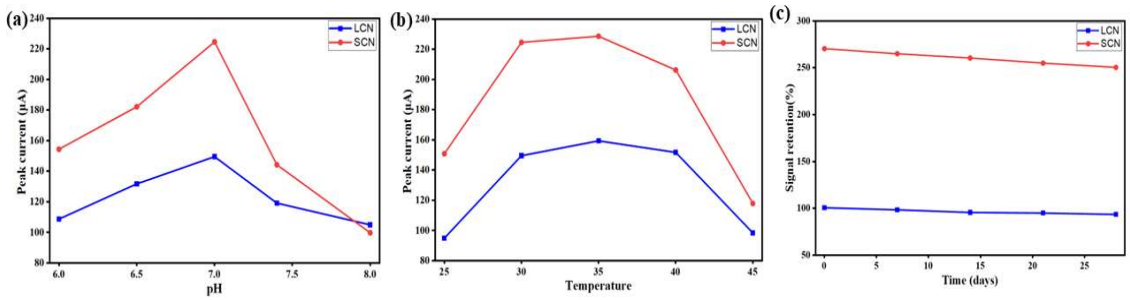

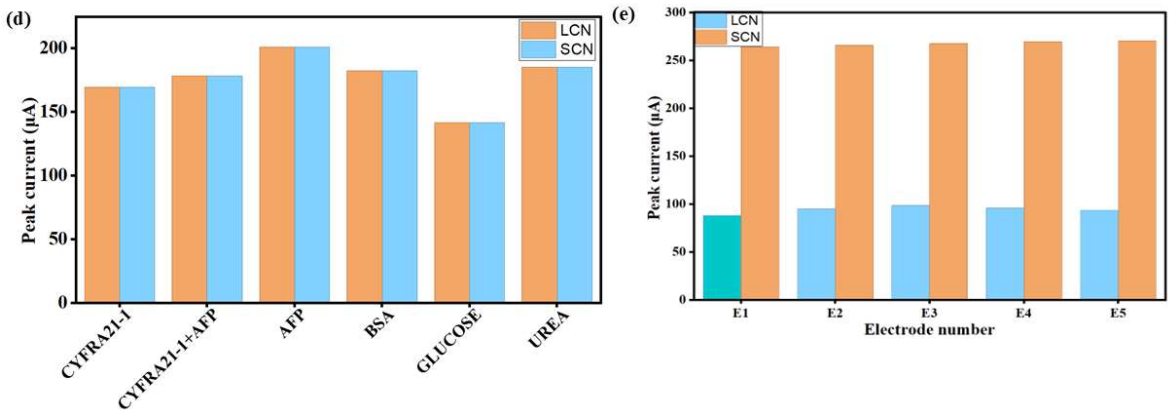

Figure 1.9. Comparative evaluation of operational performance of LCN-based and SCN-based immunosensors: (a) effect of pH, (b) effect of temperature, (c) storage stability over 28 days, (d) selectivity toward AFP in the presence of potential interfering biomolecules, and (e) reproducibility assessed using independently fabricated electrodes.

The operational parameters of the immunosensors employing LCN and SCN were modified to determine the conditions under which both sensors can potentially be comparably used for AFP detection (Figure 1.9). Both immunosensors exhibited a pH-dependent electrochemical response, with peak current values increasing at pH = 7.0, measuring 150 μA for LCN and 225 μA for SCN (Figure 1.9 (a)). the elevated peak current value correlates with excellent antigen-antibody binding and efficient electron transport across the electrode surface. The reduced electrochemical response observed with pH reduction corresponds to differences in the physiological condition of antibodies and the charge on their surface [31].

The optimization of temperature demonstrated that each system exhibited nearly comparable performance in achieving maximal electrochemical response at 35 ℃ (Figure 1.9 (b)). the increase in peak current from 25 to 35 ℃ resulted from improved diffusion and affinity interaction mechanisms of the analytes. Consequently, a current of around 160 μA was achieved for LCN, whereas SCN obtained 230 μA. The subsequent increase in temperature resulted to the decrease in the signal due to the denaturation of antibodies [32].

Studies performed under controlled conditions at 4℃ demonstrated adequate stability for more than 28 days (Figure 1.9 (c)). both the LCN sensor and SCN exhibited stability over 92%, indicating strong interfacial stability and the integrity of antibodies. As demonstrated the observation that LCN and SCN exhibit remarkable stability over the 28-day duration, it is evident that the g-C_3N_4 structure can serve as an effective foundation for biosensing.

Selectivity assays of both immunosensors against interfering substances, including CYFRA21-1, BSA, glucose, and urea, were conducted (Figure 1.9 (d)). For both sensor systems, the electrochemical response is optimized ideally for AFP, with minimal interference from other analyzed molecules. The interaction between the interferent and the target analyte (CYFRA21-1 and AFP) generated responses comparable to those obtained from AFP, indicating that signal generation mostly arises from selective binding of AFP and antibodies, rather than from non-selective adsorption onto the surface.

The reproducibility of fabrication was assessed using electrodes fabricated independently but under same conditions (Figure 1.9 (e)). The relative standard deviation (RSD) for the LCN immunosensor system was observed around 3.98% (n=6), but the SCN exhibited reduced variance, as shown by an RSD of 1.7% (n=5). The enhanced repeatability in the SCN can potentially be attributed to the uniform distribution of the SiO_2/g-C_3N_4 nanocomposites and the stable biointerface provided by the silica hydroxyl groups. These findings indicate that both immune-sensing methods provide favorable operational characteristics.

Table 1.3. Comprehensive Benchmarking of AFP Electrochemical Biosensors.

Material	Technique	Linear Range	LOD	Real Sample	Ref.
Graphene–Au	DPV	1 pg mL^{-1}–100 ng mL^{-1}	0.0196 pg mL^{-1}	N/R	[33]
PtNPs/Co_3O_4/graphene	DPV	0.1 pg mL^{-1}–60 ng mL^{-1}	0.029 pg mL^{-1}	Serum	[34]
TB–Au–Fe_3O_4–rGO	DPV	0.01 pg mL^{-1}–10 ng mL^{-1}	0.0027 pg mL^{-1}	Serum	[35]

CdTe@SiO_2/graphene	ECL	1.0 pg mL^{-1}–100 ng mL^{-1}	0.22 pg mL^{-1}	N/R	[36]
AuNPs/PGNR	CV	5–60 ng mL^{-1}	1 ng mL^{-1}	N/R	[37]
AuNPs–Dex–rGO	DPV	0.01–20 pg mL^{-1}	0.05 pg mL^{-1}	N/R	[38]
CNPs/AuNPs	DPV	0.005–1000 ng mL^{-1}	0.0019 ng mL^{-1}	N/R	[39]
Au/AET/PAMAM	CV	5–500 ng mL^{-1}	3 ng mL^{-1}	N/R	[40]
Fe_3O_4@AuNPs	EIS/DPV	1–200 ng mL^{-1}	0.65 ng mL^{-1}	N/R	[41]
Thionine–AuNPs	DPV	0.05–100 ng mL^{-1}	0.012 ng mL^{-1}	Serum	[42]
Graphene/SnO_2/Au	DPV	0.02–50 ng mL^{-1}	0.01 ng mL^{-1}	N/R	[43]
Fe_3O_4@Au@chitosan	CV	10–8000 ng mL^{-1}	1.78 ng mL^{-1}	N/R	[44]
La_2O_3/g-C_3N_4 (LCN)	CV/EIS	0.25–500 ng mL^{-1}	0.035 ng mL^{-1}	PBS	[This work]
SiO_2/g-C_3N_4 (SCN)	CV/EIS	0.25–500 ng mL^{-1}	0.0024 ng mL^{-1}	PBS	[This work]

GCE: glassy carbon electrode; SPE: screen-printed electrode; Au: gold electrode; N/R: not reported; ECL: electrochemiluminescence.

4.6. Structure-Property-Performance Correlation

The underlying trend reveals a mechanistic distinction determined by oxide chemistry. The LCN mechanism demonstrates an affinity for the point-of-care sensor based on defect-mediated heterojunction kinetics, wherein crystalline La_2O_3 nanocrystals are combined with Type-II electronic junctions of g-C_3N_4. In this instance, oxygen vacancies induced by La^{3+}ions facilitate a charge hopping mechanism, achieving nearly a 60% decrease IN Rct and a tenfold increase in k_o relative to the corresponding SCN sensor system [45]. This kinetics facilitates rapid charge transfer, resistance to fouling, and a sensitivity of 28.44 μA decade^{-1} with a limit of detection (LOD) of 0.035 ng mL^{-1}.

The presence of roughness and porosity in the SiO_2 structure, along with numerous Si-OH groups, enhances antibody adsorption and increases the accessible surface area for electrolytes, leading to a sensitivity improvement of 37.2% (39.03 μA decade^{-1}) and a 16-fold reduction in the limit of detection (LOD) to 0.00224 ng mL^{-1} compared to LCN sensor. The sensor's response predominantly depends on variations in dielectric and diffusion impedance caused by pore blockage, rather than direct alterations in kinetic processes.

In conclusion, the results mentioned above establish a framework of fundamental design concepts wherein defect—engineered heterojunction structures promote accelerated kinetics and fouling resistance, while structures with enhanced surface area are more appropriate for the highly sensitive ultrarace determination of AFP in diagnostics.

Table 1.4. Structure -Property-Performance Correlation Summary for LCN and SCN AFP Immunosensors.

Performance Metric	**LCN (La_2O_3/g-C_3N_4)**	**SCN (SiO_2/g-C_3N_4)**
Calibration equation	$\Delta Ip = 143.70 - 28.44 \log C$	$\Delta Ip = 203.33 - 39.03 \log C$
R^2 / Pearson r	0.995 / −0.997	0.998 / −0.999
Sensitivity (µA decade^{-1})	28.44	39.03
LOD (ng mL^{-1})	0.035	0.0024
LOQ (ng mL^{-1})	0.107	0.0068
Dominant sensing mechanism	Defect-mediated kinetic modulation	Pore-occlusion impedance amplification
Charge-transfer behavior	Fast heterogeneous ET; defect-assisted hopping	Diffusion- and dielectric-impedance-dominated
Reproducibility (RSD)	3.98% (n = 6)	1.7% (n = 5)
28-day stability	92.65% signal retention	92.6% signal retention
Key structural determinant	Crystalline La_2O_3 heterojunction; O-vacancy network	Amorphous SiO_2 porosity; silanol functionalization

4.7. Conclusion

The present work evaluates systematically the performance of two mechanistically different g-C_3N_4 based electrochemical sensors based on alpha-fetoprotein (AFP) for La_2O_3/g-C_3N_4 (LCN) and SiO_2/g-C_3N_4 (SCN). The LCN mechanism depends upon defect-assisted charge transfer via heterojunctions between atoms. The kinetic rate

constant (k_0 = 1.94 × 10^{-2} cm s^{-1}) increases, thus facilitating fast reactions and rendering the systems inaccessible to surface fouling. SCN enhances signal transduction by obstructing pores. This results in enhanced sensitivity (39.03 µA $decade^{-1}$) and an exceptionally low detection limit (0.0024 ng mL^{-1}) within the approved therapeutic detection range (0.25-500 ng mL^{-1}). Both systems demonstrate over 92.6% signal stability over a 28-day period, emphasizing the significance of the g-C_3N_4 matrix for prolonged sensor performance. The developed biosensor architecture provides the detection of appropriate AFP levels associated with both early and late stages of HCC, confirming the efficacy of SCN biosensors for HCC diagnosis.

Declaration of conflict interest

The authors declare that there is no known conflict of interest or personal relationships that could have appeared to influence the work reported in this paper.

Funding

Ms. Samiksha acknowledges financial support from the Council of Scientific and Industrial Research (CSIR), Government of India, under the Junior Research Fellowship (JRF) scheme (File no. 09/1063(20596)/2024-EMR-I; Ref. No: Dec-23 (i)/EU-V).

Acknowledgement

The author sincerely thanks Ms. Damini Dahiya, PhD Research Scholar, Department of CEEES, for her valuable assistance in the manuscript analysis, scientific writing, graphical figure preparation and her constructive suggestions, which significantly improved the quality of this work.

References

[1] Singh, S. P., Madke, T., & Chand, P. (2025). Global epidemiology of hepatocellular carcinoma. *Journal of clinical and experimental hepatology*, *15*(2), 102446.

[2] Singal, A. G., Kanwal, F., & Llovet, J. M. (2023). Global trends in hepatocellular carcinoma epidemiology: implications for screening, prevention and therapy. *Nature reviews Clinical oncology*, *20*(12), 864-884.

[3] Yeo, Y. H., Lee, Y. T., Tseng, H. R., Zhu, Y., You, S., Agopian, V. G., & Yang, J. D. (2024). Alpha-fetoprotein: Past, present, and future. *Hepatology Communications*, *8*(5), e0422.

[4] Baig, J. (2009). Hepatocellular carcinoma (HCC) and diagnostic significance of A-fetoprotein (AFP). *Journal of Ayub Medical College, Abbottabad: JAMC*.

[5] Li, Z., Wang, F., Liang, B., Su, Y., Sun, S., Xia, S., ... & Zheng, S. (2020). Methionine metabolism in chronic liver diseases: an update on molecular mechanism and therapeutic implication. *Signal transduction and targeted therapy*, *5*(1), 280.

[6] Wan, Y., Su, Y., Zhu, X., Liu, G., & Fan, C. (2013). Development of electrochemical immunosensors towards point of care diagnostics. *Biosensors and Bioelectronics*, *47*, 1-11.

[7] Hou, F., Sun, S., Abdullah, S. W., Tang, Y., Li, X., & Guo, H. (2023). The application of nanoparticles in point-of-care testing (POCT) immunoassays. *Analytical Methods*, *15*(18), 2154-2180.

[8] Sandhyarani, N. (2019). Surface modification methods for electrochemical biosensors. In *Electrochemical biosensors* (pp. 45-75). Elsevier.

[9] Zheng, M., Li, W., Ma, F., & Liang, M. (2025). Graphitic carbon nitride-based materials: applications in medical diagnostics, therapeutics, and combined cancer therapies. *Journal of Materials Chemistry C*, *13*(34), 17483-17536.

[10] Yin, C., Liu, Y., Hu, T., & Chen, X. (2025). Graphitic carbon nitride nanomaterials-based electrochemical sensing interfaces for monitoring heavy metal ions in aqueous environments. *Nanomaterials*, *15*(7), 564.

[11] Xavier, M. M., Nair, P. R., & Mathew, S. (2019). Emerging trends in sensors based on carbon nitride materials. *Analyst*, *144*(5), 1475-1491.

[12] Chen, J., Hou, Y., & Li, G. (2025). Synergistic regulation of hydrogen trapping-diffusion at grain boundaries and interfacial hydrogen resistance in La_2O_3/Y-doped Cr_2O_3-based coatings. *Surface and Coatings Technology*, *513*, 132464.

[13] Anand, L. G. (2026). Hydrothermal Synthesis and Structural Characterization of Lanthanum Oxide (La_2O_3) Nanorods.

[14] El Shafei, G. M. (2000). Silica surface chemical properties. *Surfactant Science Series*, 35-62.

[15] Alba Martín, M. (2014). Silicon dioxide microstructures based on macroporous silicon for biomedical applications.

[16] Antil, S., & Singh, S. (2026). Novel La_2O_3/g-C_3N_4 Nanocomposite Electrochemical Immunosensor for Sensitive Detection of Alpha-Fetoprotein in Hepatocellular Carcinoma. *Analytical Letters*, 1-22.

[17] Antil, S., & Singh, S. (2026). SiO_2/g-C_3N_4 Nanocomposite-enabled immunosensor platform for high-fidelity electrochemical platform for high-fidelity electrochemical detection of alpha-fetoprotein. *Genetics and Molecular Research*.

[18] Jasni, N., Iqbal, A., Ahmad, M. N., Pauzi, H., & Hussain, M. H. (2022). Synthesis and characterisation of Li-modified g-C3N4. *Materials Today: Proceedings*, *57*, 1154-1161.

[19] Mu, Q., & Wang, Y. (2011). Synthesis, characterization, shape-preserved transformation, and optical properties of $La(OH)_3$, $La_2O_2CO_3$, and La_2O_3 nanorods. *Journal of alloys and compounds*, *509*(2), 396-401.

[20] Dubey, R. S., Rajesh, Y. B. R. D., & More, M. A. (2015). Synthesis and characterization of SiO_2 nanoparticles via sol-gel method for industrial applications. *Materials Today: Proceedings*, *2*(4-5),

3575-3579.
[21] Chin, J. Y., Ahmad, A. L., & Low, S. C. (2023). Graphitic carbon nitride photocatalyst for the degradation of oxytetracycline hydrochloride in water. *Materials Chemistry and Physics*, *301*, 127626.
[22] Karthikeyan, S., Parthibavarman, M., Mohammed, M. K., Mohammed, S. H., Selvapandiyan, M., & Srisuvetha, V. T. (2022). Morphology and vibrational modes of lanthanum oxide (La_2O_3) nanoparticles prepared with reflux routes at different reaction times. *Chemistry Africa*, *5*(5), 1427-1432.
[23] Saravanan, S., & Dubey, R. S. (2020). Synthesis of SiO_2 nanoparticles by sol-gel method and their optical and structural properties. *Rom. J. Inf. Sci. Technol*, *23*(1), 105-112.
[24] Karthikeyan, S., Dhanakodi, K., Surendhiran, S., Jagan, K. S. G., Thirunavukkarasu, P., & Arunraja, L. (2023). Effect of synthesis parameters on the structural, morphological characteristics, and photocatalytic activity of La_2O_3 nanoparticles. *Journal of the Indian Chemical Society*, *100*(1), 100860.
[25] Nandanwar, R., Singh, P., & Haque, F. Z. (2015). Synthesis and characterization of SiO_2 nanoparticles by sol-gel process and its degradation of methylene blue. *Am. Chem. Sci. J*, *5*(1), 1-10.
[26] Ong, W. J., Tan, L. L., Ng, Y. H., Yong, S. T., & Chai, S. P. (2016). Graphitic carbon nitride (g-C_3N_4)-based photocatalysts for artificial photosynthesis and environmental remediation: are we a step closer to achieving sustainability. *Chemical reviews*, *116*(12), 7159-7329.
[27] Bhautik, M. P. N., Ugwekara, R. P., & Singhb, M. K. Review on synthesis of Lanthanum oxide (La_2O_3) and characterization techniques.
[28] Taing, M. H. (2009). Characterisation and Fabrication of a Multiarray Electrolyte-insulator-semiconductor Biosensor.
[29] Li, Y., Liu, J., Chen, X., Yuan, X., Li, N., He, W., & Feng, Y. (2020). Enhanced electricity generation and extracellular electron transfer by polydopamine–reduced graphene oxide (PDA–rGO) modification for high-performance anode in microbial fuel cell. *Chemical Engineering Journal*, *387*, 123408.
[30] Sharafeldin, M., McCaffrey, K., & Rusling, J. F. (2019). Influence of antibody immobilization strategy on carbon electrode immunoarrays. *Analyst*, *144*(17), 5108-5116.
[31] Ruiz, G., Tripathi, K., Okyem, S., & Driskell, J. D. (2019). pH impacts the orientation of antibody adsorbed onto gold nanoparticles. *Bioconjugate chemistry*, *30*(4), 1182-1191.
[32] Vermeer, A. W., & Norde, W. (2000). The thermal stability of immunoglobulin: unfolding and aggregation of a multi-domain protein. *Biophysical journal*, *78*(1), 394-404.
[33] Shan, J., Wang, L., and Ma, Z. (2016). Novel metal-organic nanocomposites: Poly (methylene blue)-Au and its application for an ultrasensitive electrochemical immunosensing platform. *Sensors and Actuators B: Chemical*, *237*, 666-671.
[34] Liu, L., Tian, L., Zhao, G., Huang, Y., Wei, Q., and Cao, W. (2017). Ultrasensitive electrochemical immunosensor for alpha fetoprotein detection based on platinum nanoparticles anchored on cobalt oxide/graphene nanosheets for signal amplification. *Analytica chimica acta*, *986*, 138-144.
[35] Wang, Y., Zhang, Y., Wu, D., Ma, H., Pang, X., Fan, D., and Du, B. (2017). Ultrasensitive label-free electrochemical immunosensor based on multifunctionalized graphene nanocomposites for the detection of alpha fetoprotein. *Scientific Reports*, *7*(1), 42361.
[36] Pan, D., Chen, K., Zhou, Q., Zhao, J., Xue, H., Zhang, Y., and Shen, Y. (2019). Engineering of CdTe/SiO_2 nanocomposites: Enhanced signal amplification and biocompatibility for electrochemiluminescent immunoassay of alpha-fetoprotein. *Biosensors and Bioelectronics*, *131*, 178-184.
[37] Jothi, L., Jaganathan, S. K., and Nageswaran, G. (2020). An electrodeposited Au nanoparticle/porous graphene nanoribbon composite for electrochemical detection of alpha-fetoprotein. *Materials Chemistry and Physics*, *242*, 122514.
[38] Zhou, J., Zhang, C., Chen, Y., Wang, Z., Lan, L., Wang, Y., and Chen, Q. (2019). A simple immunosensor for alpha-fetoprotein determination based on gold nanoparticles-dextran-reduced graphene oxide. *Journal of Electroanalytical Chemistry*, *833*, 126-132.
[39] Idris, A. O., Mabuba, N., and Arotiba, O. A. (2018). An alpha-fetoprotein electrochemical immunosensor based on a carbon/gold bi-nanoparticle platform. *Analytical Methods*, *10*(47), 5649-5658.
[40] Giannetto, M., Elviri, L., Careri, M., Mangia, A., and Mori, G. (2011). A voltammetric immunosensor based on nanobiocomposite materials for the determination of alpha-fetoprotein in serum. *Biosensors and Bioelectronics*, *26*(5), 2232-2236.
[41] Liang, R. P., Yao, G. H., Fan, L. X., and Qiu, J. D. (2012). Magnetic Fe_3O_4@ Au composite-enhanced surface plasmon resonance for ultrasensitive detection of magnetic nanoparticle-enriched α-fetoprotein. *Analytica chimica acta*, *737*, 22-28.
[42] Alizadeh, N., Salimi, A., and Hallaj, R. (2018). Magnetoimmunosensor for simultaneous electrochemical detection of carcinoembryonic antigen and α-fetoprotein using multifunctionalized Au nanotags. *Journal of Electroanalytical Chemistry*, *811*, 8-15.
[43] Liu, J., Lin, G., Xiao, C., Xue, Y., Yang, A., Ren, H., and Yuan, Z. (2015). Sensitive electrochemical immunosensor for α-fetoprotein based on graphene/SnO_2/Au nanocomposite. *Biosensors and Bioelectronics*, *71*, 82-87.
[44] Li, S., Liang, J., Zhou, Z., and Li, G. (2018, July). An electrochemical immunosensor for AFP measurement based on the magnetic Fe_3O_4@ Au@ CS

nanomaterials. In *IOP Conference Series: Materials Science and Engineering* (Vol. 382, No. 2, p. 022017). IOP Publishing.
[45] Siddique, M. N., & Tripathi, P. (2022). Influence of La^{3+} ion doping on electrical conduction and thermal stability of NiO nanostructures. *Materials Chemistry and Physics*, *277*, 125612.